

## Cite this article

Jia T, Stanier S, Watson P, Feng X and Gourvenec S (2023)  
The effect of soil type on the behaviour of a tolerably mobile subsea foundation.  
*International Journal of Physical Modelling in Geotechnics* **23(6)**: 273–292,  
<https://doi.org/10.1680/jphmg.22.00017>

## Research Article

**Paper 2200017**  
Received 03/04/2022;  
Accepted 06/12/2022;  
First published online 21/12/2022

Emerald Publishing Limited: All rights reserved

# The effect of soil type on the behaviour of a tolerably mobile subsea foundation

## Tianqiang Jia PhD

Geotechnical Engineer, Ocean Graduate School, University of Western Australia, Perth, Australia (corresponding author: 22370683@student.uwa.edu.au, jtq2016uwa@gmail.com)

## Sam Stanier PhD

Senior Lecturer, Department of Engineering, University of Cambridge, Cambridge, UK

## Phil Watson PhD

Professor, Ocean Graduate School, University of Western Australia, Perth, Australia

## Xiaowei Feng PhD

Professor, Faculty of Infrastructure Engineering, Dalian University of Technology, Dalian, China

## Susan Gourvenec PhD

Professor, School of Engineering, University of Southampton, Southampton, UK



Tolerably mobile subsea foundations may be used to replace conventional fixed mudmat foundations for pipeline infrastructure and are designed to slide on the seabed along with the connected pipeline, in order to accommodate thermally induced horizontal forces. This allows the size of the foundation and the resulting fabrication and installation costs to be substantially reduced. The performance of mobile foundations is explored in this paper through four centrifuge model tests on a normally consolidated or lightly over-consolidated reconstituted calcareous silt obtained from the Northwest Shelf of Western Australia. The results are compared to three existing tests performed on a kaolin clay. The results show that under typical periodic surface sliding and intervening rests, sliding resistance evolves within a cycle with resistance peaks evident at either end of the sliding footprint due to the formation of berms, and the residual resistance increasing with sliding cycles towards a drained state. Shear and consolidation-induced settlements accumulate with sliding cycles although at a reducing rate. The tests in the calcareous silt show higher normalised initial peak sliding resistance, a more dramatic loss and slower recovery of sliding resistance with cycles, and slower rate of decrease of incremental settlement compared with the response in kaolin clay.

**Keywords:** calcareous soils/centrifuge modelling/shallow foundations/UN SDG 9: Industry, innovation and infrastructure

## Notation

$B$	breadth of the foundation	$N_c$	vertical bearing capacity factor
$c_h$	horizontal coefficient of consolidation	$R_{cpt}$	radius of piezocone penetration test
$c_{ref}$	representative coefficient of consolidation	$S_t$	soil sensitivity measured by T-bar
$D_{T-bar}$	diameter of T-bar	$S_{t,r}$	real undrained shear strength ratio
$d_{50}$	mean effective particle size	$s_{u,cyc}$	undrained shear strength measured by T-bar at the present cycle
$e$	void ratio	$s_{u,n=0}$	true undisturbed undrained shear strength of the 0th cycle
$e_{LL}$	void ratio at liquid limit (LL)	$s_{u,n=0.25}$	undrained shear strength measured by T-bar at the 0.25th cycle
$e_N$	void ratio intercept of normal compression line (NCL) at $\sigma'_v = 1$ kPa	$s_{u,m}$	undrained shear strength at mudline
$G_s$	specific gravity	$t$	time
$h$	thickness of the foundation	$t_{con}$	consolidation time
$I_r$	rigid index	$V_{eff}$	effective vertical load
$L$	length of the foundation	$V_{op}$	vertical operational load
$m_c$	moisture content	$V_{ult}$	ultimate vertical bearing capacity
$N$	number of cycle		

$V_{ult0}$	initial ultimate vertical bearing capacity
$w$	settlement of the mudmat
$w_{con}$	consolidation settlement of the mudmat
$w_p$	shear settlement of the mudmat
$(s_u/\sigma'_v)_{NC}$	undrained shear strength ratio measured by T-bar
$(s_u/\sigma'_v)_{NC,r}$	real undrained shear strength ratio
$\gamma'$	submerged unit weight
$\gamma_w$	unit weight of water
$\delta$	sliding distance
$\delta_{50}$	sliding distance that the soil softens to 50% of its peak undrained shear strength
$\delta_{95}$	sliding distance that the soil softens to 95% of its peak undrained shear strength
$\theta_{mat}$	slope of the skis of the foundation
$\kappa$	slope of unloading–reloading line
$\lambda$	slope of NCL
$\mu$	friction coefficient
$\sigma'_v$	vertical effective stress
$\sigma'_{v,sur}$	surcharge pressure
$(\sigma'_v)_{NCL}$	effective stress on NCL
$\phi$	friction angle

## 1. Introduction

In contrast to conventional fixed subsea shallow foundations used for pipeline end terminations (PLETs), tolerably mobile subsea foundations (Bretelle and Wallerand, 2013; Cathie *et al.*, 2008; Cocjin *et al.*, 2014, 2017; Corti *et al.*, 2017; Deeks *et al.*, 2014; Gourvenec and Feng, 2014; Randolph *et al.*, 2011; Wallerand *et al.*, 2015) are engineered to slide across the seabed within allowable limits to accommodate the thermal forces built up in pipelines, thereby creating the potential to reduce the foundation footprint (Randolph *et al.*, 2011). As well as a direct reduction in material cost, the relatively small size and simple geometry make fabrication and installation of tolerably mobile foundations easier and cheaper (Cocjin, 2016). Tolerably mobile subsea foundations have been deployed offshore (Deeks *et al.*, 2014), although all known installations are not reported in the public domain. The load paths and response of tolerably mobile shallow foundations are potentially complex, including eccentricity of self-weight and torsional shear forces, but whole-life sliding resistance and settlement under planar sliding are of most significance and considered in this study.

Previous centrifuge model tests have been performed (Blanc *et al.*, 2016; Cocjin *et al.*, 2014; Stuyts *et al.*, 2015; Wallerand *et al.*, 2015) and greatly improved the general understanding of how mobile foundations behave, as well as providing benchmarks for theoretical research. The centrifuge testing on a lightly over-consolidated (LOC) kaolin clay performed by Cocjin *et al.* (2014) indicates that the sliding resistance would

increase throughout the whole-life periodic movements after a significant drop at the first slide, and that the settlement accumulates throughout the operational life, albeit at a decreasing rate. The whole-life settlement is minimised by adopting a smoother foundation–soil interface, although the trade-off is that the sliding resistance is lower and infrastructure supported by smoother foundations is freer to move. The greatest effects on increased sliding resistance and settlement are observed in normally consolidated (NC) deposits, as would be expected.

The purpose of this study was to understand how sliding response differs in different soils, through centrifuge testing on a calcareous silt and comparing it with the previous tests performed on a kaolin clay as given by Cocjin *et al.* (2014). The calcareous silt, which was obtained from the North West Shelf (NWS) of Western Australia, exhibits higher sensitivity and strength ratio and lower coefficient of consolidation than the clay, with four model tests carried out in the silt as part of the current study.

## 2. Experimental apparatus

### 2.1 Centrifuge facilities

All tests were conducted at 100g in a fixed beam centrifuge with a nominal radius of 1.8 m (Randolph *et al.*, 1991). Tests were conducted in an aluminium strong box with internal dimensions of 390 × 650 × 300 mm in breadth, length and height, respectively. A two-axis actuator attached to the strong box using aluminium crossbars was used to control the load applied to the foundation and its lateral position during the test (after O'Loughlin *et al.* (2018)). Figure 1(a) provides an overview of the experimental set-up.

### 2.2 Loading and acquisition system

The loading and monitoring system consisted of actuators that control the horizontal and vertical displacement of the foundation, sensors and lasers that were used to measure displacement and rotation, with a frame connecting the actuator and the foundation to transmit the applied loads, as shown in Figure 1(b). The foundation was displacement controlled in horizontal and load controlled in vertical orientations. Through the roller within the loading arm and the hinged joint above the foundation (Figure 1(c)), rotation of the foundation was allowed about both the short and long axis. More details of the loading and acquisition system are available in the paper by Cocjin *et al.* (2014).

### 2.3 Model mudmat foundation

The rigid model foundation is made from acetal and is shown in Figures 1(c) and 1(d) – comprising a rectangular base plate that is 50 mm in breadth ( $B = 50$  mm), 100 mm long ( $L = 100$  mm) and has thickness of 5 mm ( $h = 5$  mm). The sides of the foundation include 30° skis ( $\theta_{mat} = 30^\circ$ ) to promote sliding over (rather than cutting into) the surface soil during

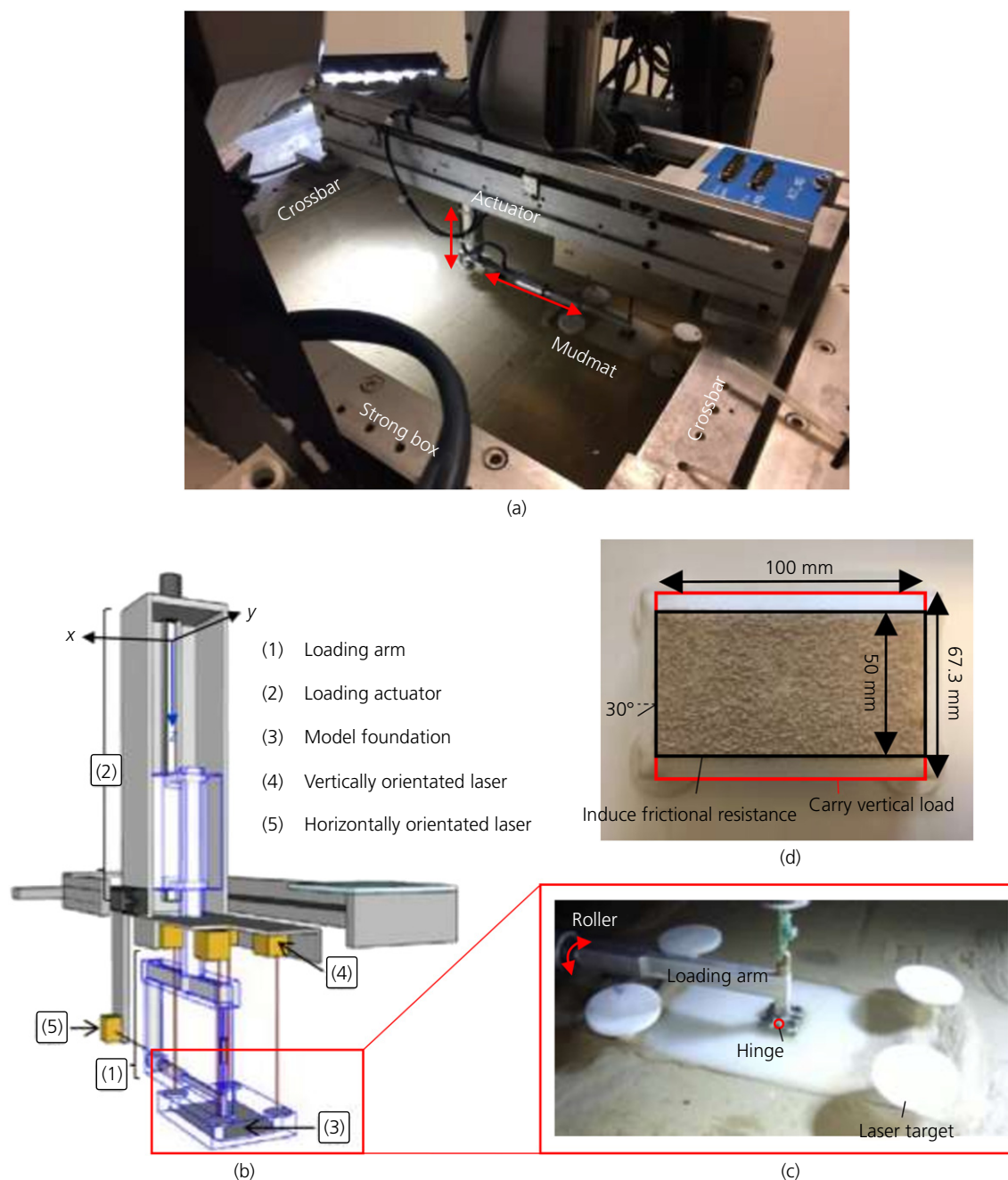


**Figure 1.** Experimental set-up: (a) apparatus set-up; (b) schematic of loading and measuring system (O'Loughlin *et al.*, 2018); (c) model foundation and the connected loading arm; (d) view from foundation base

movement. Based on previous testing experience, coarse silica sand ( $D_{50} = 0.544$  mm) was glued to the foundation base using epoxy resin – to create a rough interface and ensure that failure yields in the underlying soil instead of along the interface so that soil behaviours can be clearly measured. Four round plates were attached to corners of the top plate as

targets for an array of laser transducers, used to measure the settlement, pitch and roll of the foundation during testing. Consistent with designs used in practice, the loading point was set as low as possible to minimise overturning moment in the direction of loading, with the hinge placed at 5 mm ( $5\%L$ ) above the centre of the top plate. The same foundation was

also used by Cocjin *et al.* (2014) whose test results are compared to the tests presented in this paper.

### 3. Soil properties

#### 3.1 Review of properties

The basic properties of the calcareous silt used in this paper are listed and compared with the kaolin clay in Table 1. The kaolin clay has been widely tested by other researchers (Cocjin *et al.*, 2014; Lehané *et al.*, 2009; Sahdi *et al.*, 2014a, 2014b, 2016; Stewart, 1992; Zhou *et al.*, 2019). The calcareous silt used in this study has been tested at the University of Western Australia and the properties reported by Chow *et al.* (2019) and Zhou *et al.* (2020a, 2020b) show consistency between experiments. The calcareous silt exhibits a larger internal friction angle ( $\phi = 40^\circ$ ) than the kaolin clay, which is reported to be about  $23.5^\circ$  (Stewart, 1992).

#### 3.2 Sample preparation

The calcareous silt was initially mixed with water to twice its liquid limit (LL) ( $\sim 145\%$ ). The slurry was subsequently mixed under vacuum over a period of 48 h before it was poured into the strong box on top of a 10 mm thick sand and porous fabric membrane to facilitate adequate drainage at the base of the sample during consolidation. Before being consolidated in the centrifuge for a further 72 h, the soil sample in the strong box was left on the laboratory floor for 72 h to allow the soil to settle, which helps to avoid segregation during consolidation. Given the potential for small changes in strength to impact the results of testing lightweight foundations, it was important to ensure the sample was fully consolidated. Accordingly, T-bar tests were then performed over 5 days – and model testing only commenced once the increase in the T-bar tip resistance between sequential tests was within 5%.

**Table 1.** Properties of the kaolin clay and the carbonate silt in references

Property	Clay	Silt
Internal friction angle, $\phi$ : $^\circ$	23.5	40
Strength factor of high stress level, $M_0 = 6 \sin \phi / (3 - \sin \phi)$ : dimensionless	0.92	1.62
Slope of normal compression line in $e - \ln \sigma'_v$ plane, $\lambda$ : dimensionless	0.205–0.31	0.287
Slope of swelling line in $e - \ln \sigma'_v$ plane, $\kappa$ : dimensionless	0.044–0.06	0.036
The void ratio intercept of NCL at $\sigma'_v = 1$ kPa, $e_N$ : dimensionless	3.40–3.72	4.00
LL: dimensionless	0.61	0.67
Plastic limit: dimensionless	0.27	0.39
Specific gravity, $G_s$ : dimensionless	2.6	2.71

The basin-shape surface of the soil sample (due to the Coriolis effect) was subsequently scraped between 4 and 24 mm in order to achieve a flat surface for subsequent model testing, before being reconsolidated for a period of at least 24 h prior to further model foundation testing. As the scraping was not uniform across the soil surface, the calculated over-consolidation ratio (OCR) varies slightly across each footprint – the effect of this is expected to be negligible, with the surcharge pressure at the testing footprint lying between 2 and 6 kPa.

#### 3.3 Submerged unit weight

The submerged unit weight  $\gamma'$  was calculated from Equation 1 using the moisture content ( $m_c$ ) measured from 20 mm dia. sample cores extracted from the centrifuge sample (Figure 2).

$$1. \quad \gamma' = \frac{(G_s - 1)\gamma_w}{1 + m_c G_s}$$

where  $G_s$  is the specific gravity;  $\gamma_w$  is the unit weight of water. The distribution of submerged unit weight along depth for silt and clay is exhibited in Figure 3 in prototype scale. The average submerged unit weight in the upper 1B (5 m in prototype) is 4.7 and 5.5 kN/m<sup>3</sup> for the calcareous silt and the kaolin clay, respectively.

#### 3.4 Compression characteristics

The normal compression line in the  $e - \sigma'_v$  plane can be derived from the sample core data, which were taken after scraping, and hence the void ratio and its corresponding effective stress need to be slightly adjusted by OCR ( $= \sigma'_{v,c} / \sigma'_v$ ) through the equations below:

$$2. \quad e = G_s m_c - \kappa \ln(\text{OCR})$$

$$3. \quad \sigma'_{v,c} = \gamma' z + \sigma'_{v,\text{sur}}$$

where  $\kappa$  is the slope of unloading–reloading line,  $\sigma'_{v,c}$  is the pre-consolidated pressure prior to scraping and  $\sigma'_{v,\text{sur}}$  is the surcharge pressure, which is estimated to be 5 kPa for the amount scraped from the samples taken at around the edge of the strong box. The normal compression line for the calcareous silt is shown in Figure 4 and compared with the kaolin clay (Cocjin *et al.*, 2017). The calcareous silt shows a linear relationship between void ratio and vertical effective stress (ln scale) as depicted through conventional theory, with the slope of the compression line ( $\lambda = 0.287$ ) given by Chow *et al.* (2019) fitting the measurements derived from the sample core. In comparison, the normal compression line of the kaolin clay is

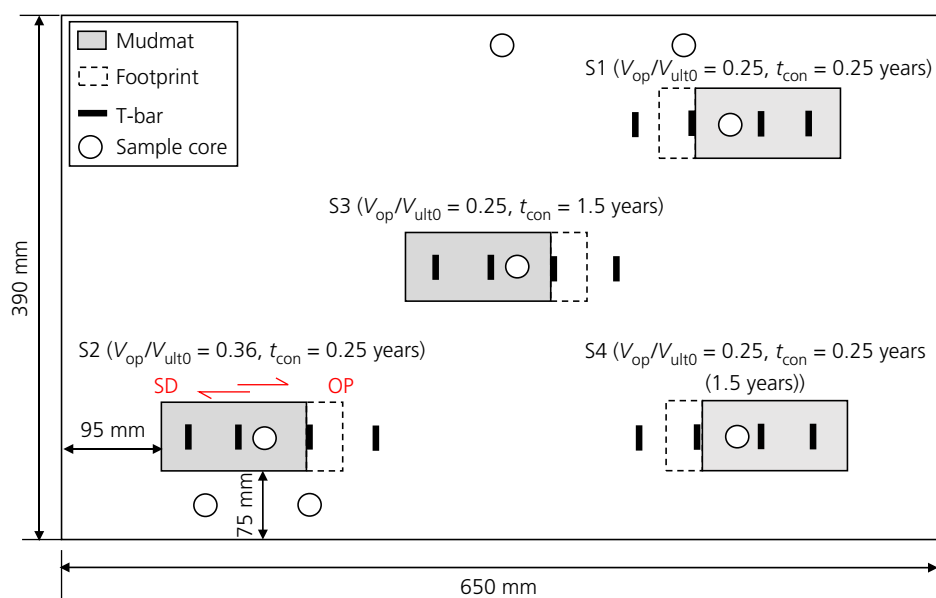


Figure 2. Schematic of test plan

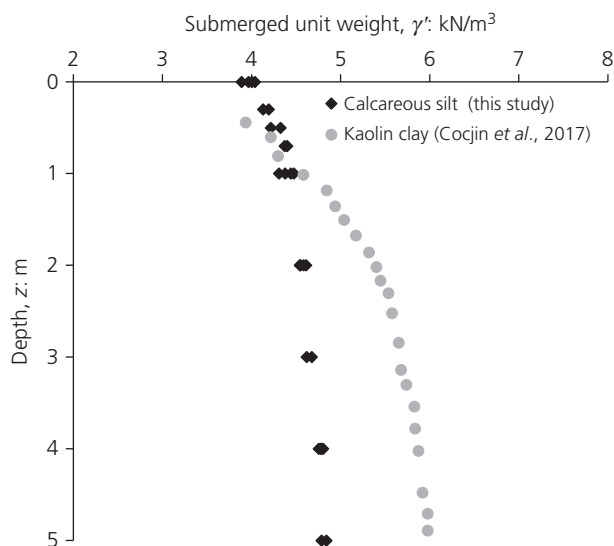


Figure 3. Distribution of submerged unit weight along depth for the calcareous silt and the kaolin clay

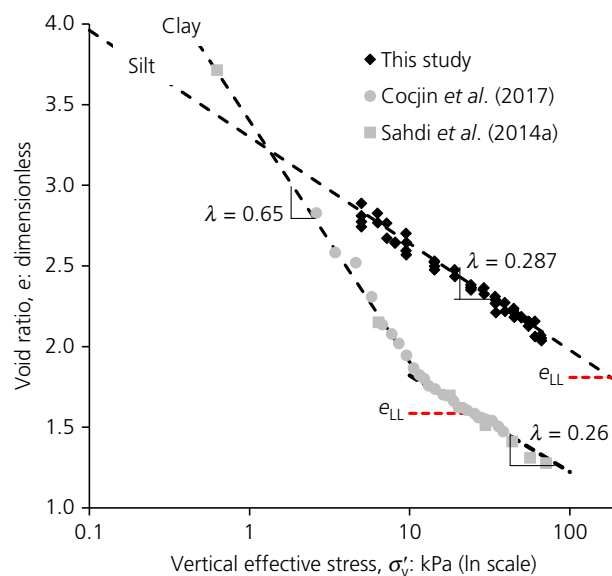


Figure 4. Void ratio plotted against vertical effective stress: compressibility of the calcareous silt and the kaolin clay

bi-linear, with a higher slope ( $\lambda = 0.65$ ) at low stress levels and a lower value ( $\lambda = 0.26$ ) at high stress levels (Cocjin *et al.*, 2017; Sahdi *et al.*, 2014a). The ‘bi-linear’ characteristic has been widely observed in many clay soils (Nagaraj *et al.*, 1998; Sun *et al.*, 2016) with the turning point observed to be around the LL, with the corresponding void ratio termed as  $e_{LL}$ .

### 3.5 Consolidation characteristics

A piezocone penetration (CPTu) dissipation test was performed at three depths (4.2, 8.2 and 10.2 m at prototype scale) to determine the horizontal coefficient of consolidation  $c_h$ . The non-dimensional consolidation time was calculated after

Teh and Houlsby (1991) as

$$4. \quad T = \frac{c_h t}{R_{\text{cpt}}^2 I_r^{0.5}}$$

where  $R_{\text{cpt}} = 5$  mm is the radius of the cone and  $I_r = 100$  is rigid index as provided by Chow *et al.* (2019). The dissipation tests were interpreted using the methodology given by Sully *et al.* (1999) and compared with results from finite-element analysis as shown in Figure 5(a). The derived  $c_h$  values at the three depths were plotted in Figure 5(c) against the vertical effective stress  $\sigma'_v$ .

Piezo-foundation tests were used to measure near-surface dissipation characteristics, and are considered to be more representative of the drainage conditions beneath a mudmat (Cocjin *et al.*, 2014). The representative coefficient of consolidation  $c_{\text{ref}}$  can be obtained by comparing the normalised dissipation curve shown in Figure 5(b) with the result from finite-element analysis (Gourvenec and Randolph, 2010). The derived coefficient of consolidation for two different effective stress levels is presented in Figure 5(c), showing that  $c_{\text{ref}}$  is around 1/3  $c_h$ . The  $c_{\text{ref}}$  for kaolin clay is plotted in Figure 5(c) for comparison, with both soils fitted using a power-law relationship. The fitting equation of the kaolin clay was given by Cocjin *et al.* (2014) as

$$5. \quad c_{\text{ref}} = 2.7[0.3 + 0.16(\sigma'_{v\text{NCL}})]^{0.47}$$

A similar equation for the silt is

$$6. \quad c_{\text{ref}} = 0.33[(\sigma'_{v\text{NCL}})]^{0.47}$$

where  $(\sigma'_{v\text{NCL}})$  is the effective stress on the normal compression line (NCL).

### 3.6 Undrained shear strength characteristics

Cyclic T-bar tests (Stewart, 1991; Stewart and Randolph, 1994) were performed in virgin soil outside of the proposed sliding footprint (Figure 2). The soil shear strength profile shown in Figure 6(a) was derived from a typical T-bar test using a penetration rate of 1 mm/s. Ten cycles of cyclic penetration and extraction were performed between the depths of 6.5 and 8.5 m (in prototype scale), equivalent to 13–17  $D_{\text{T-bar}}$ , where  $D_{\text{T-bar}} = 0.5$  m (in prototype scale) is the diameter of T-bar. The in situ strength profile was interpreted according to the methodology of White *et al.* (2010), showing the gradient of strength with depth to be around 2 kPa/m – which is consistent with the previous studies (Chow *et al.*, 2019; Zhou *et al.*, 2020a, 2020b). The NC strength ratio  $(s_u/\sigma'_{v\text{NC}})$  was

back-calculated from the initial strength profile using Equation 7 as proposed by Wroth (1984). The average submerged unit weight was 4.7 kN/m<sup>3</sup> and the undrained shear strength stress ratio  $(s_u/\sigma'_{v\text{NC}})$  was 0.42.

$$7. \quad s_u = \sigma'_v \left( \frac{s_u}{\sigma'_v} \right)_{\text{NC}} \text{OCR}^{(\lambda-\kappa)/\lambda}$$

Strength degradation for the calcareous silt and kaolin clay is compared in Figure 6(c). Sensitivity was measured by the T-bar ( $S_t$ ) to be 4.1 for the calcareous silt, and compares to around 2.5 for the kaolin clay, as reported by Cocjin *et al.* (2014).

A number of studies have revealed that the undrained shear strength degrades exponentially with T-bar penetration cycle number with the initial undrained shear strength measured by the T-bar penetrometer being accounted for as the strength after 0.25 cycles of remoulding, denoted as  $s_{u,n=0.25}$  (Sahdi, 2013; Zhou and Randolph, 2009a, 2009b). The intact undrained shear strength denoted as  $s_{u,n=0}$  (strength at 0th cycle) should be back-calculated through the degradation curve (Zhou and Randolph, 2009b). The values of  $s_{u,n=0}$  and  $s_{u,n=0.25}$  for the silt are compared in Figure 6(a). The ‘real’ strength ratio  $(s_u/\sigma'_{v\text{NC},r})$  and ‘real’ sensitivity  $S_{t,r}$  were 0.57 and 4.8 for the calcareous silt, respectively, and 0.20 and 3.1 for clay. In essence, these higher values are representative of the undrained strength ratios that might be determined from element tests, where mobilisation-induced remoulding is less of an issue.

An equivalent long-term cyclic T-bar test was conducted in the silt, as shown in Figure 6(b). The test comprised 50 cycles of full penetration and extraction with 780 s (0.25 years in prototype) consolidation time between each cycle allowing for full dissipation of excess pore pressure. The strength variation factor  $(s_{u,\text{cyc}}/s_{u,n=0.25})$  at the deepest penetration depth is plotted in Figure 6(d) and compared with that of the kaolin clay given by Cocjin *et al.* (2014). It can be observed that the silt recovers its strength more slowly than the kaolin clay, eventually reaching a steady value which is around 1.8 times the initial strength – and which is regarded as its drained state (i.e. no more excess pore-pressure generation and dissipation in spite of further deformation at undrained rates). In contrast, the kaolin clay appears to approach an asymptote at around 3 times the initial strength.

## 4. Test plan

Four model tests (S1–S4) were planned in the calcareous silt sample at the locations shown in Figure 2. The distance of at least 1B was given between each test footprint and to the edges of the strong box to minimise the influence from other tests and the boundaries. Tests were planned in the number order to give the

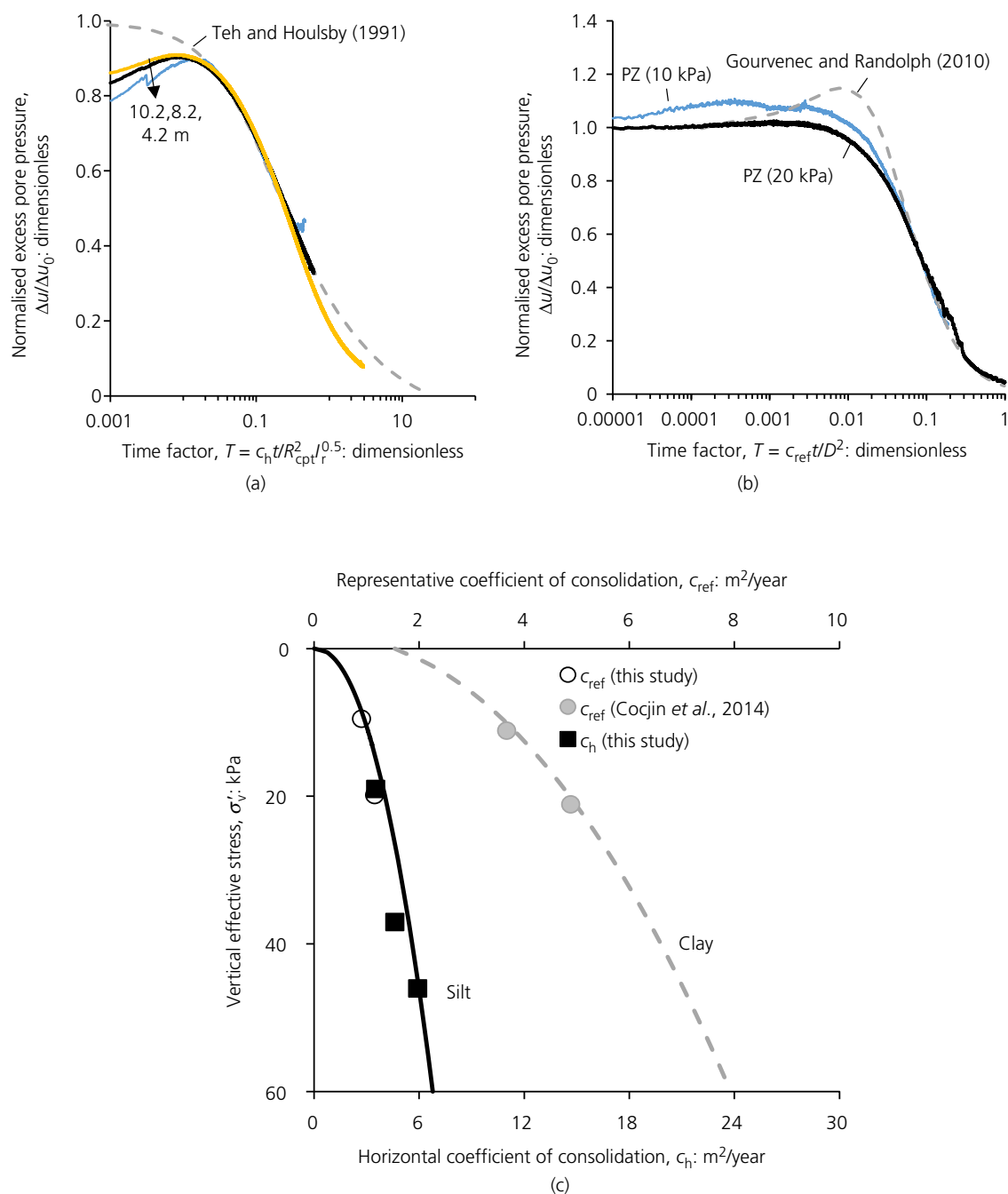


**Figure 5.** Consolidation tests performed using CPTu and piezo-foundation: (a) dissipation curves of the calcareous silt tested by CPTu at 4.2, 8.2 and 10.2 m in prototype; (b) dissipation curves of the calcareous silt tested by piezo-foundation (PZ) under the vertical stress of 10 and 20 kPa; (c) coefficient of consolidation of the calcareous silt and the kaolin clay

area time to return to equilibrium before conducting the next test. A representative sliding distance of  $0.25L$  was applied to each test, which is sufficient to mobilise steady-state sliding failure. After each test, sampling and T-bar testing were conducted to measure distributions of moisture content and strength at the footprint.

## 5. Test procedure

During each test, free water was maintained above the soil surface at a (constant) level deep enough to fully submerge the mudmat, but not the attached laser targets. As the foundation settles a slight change in buoyancy occurs, as the submerged

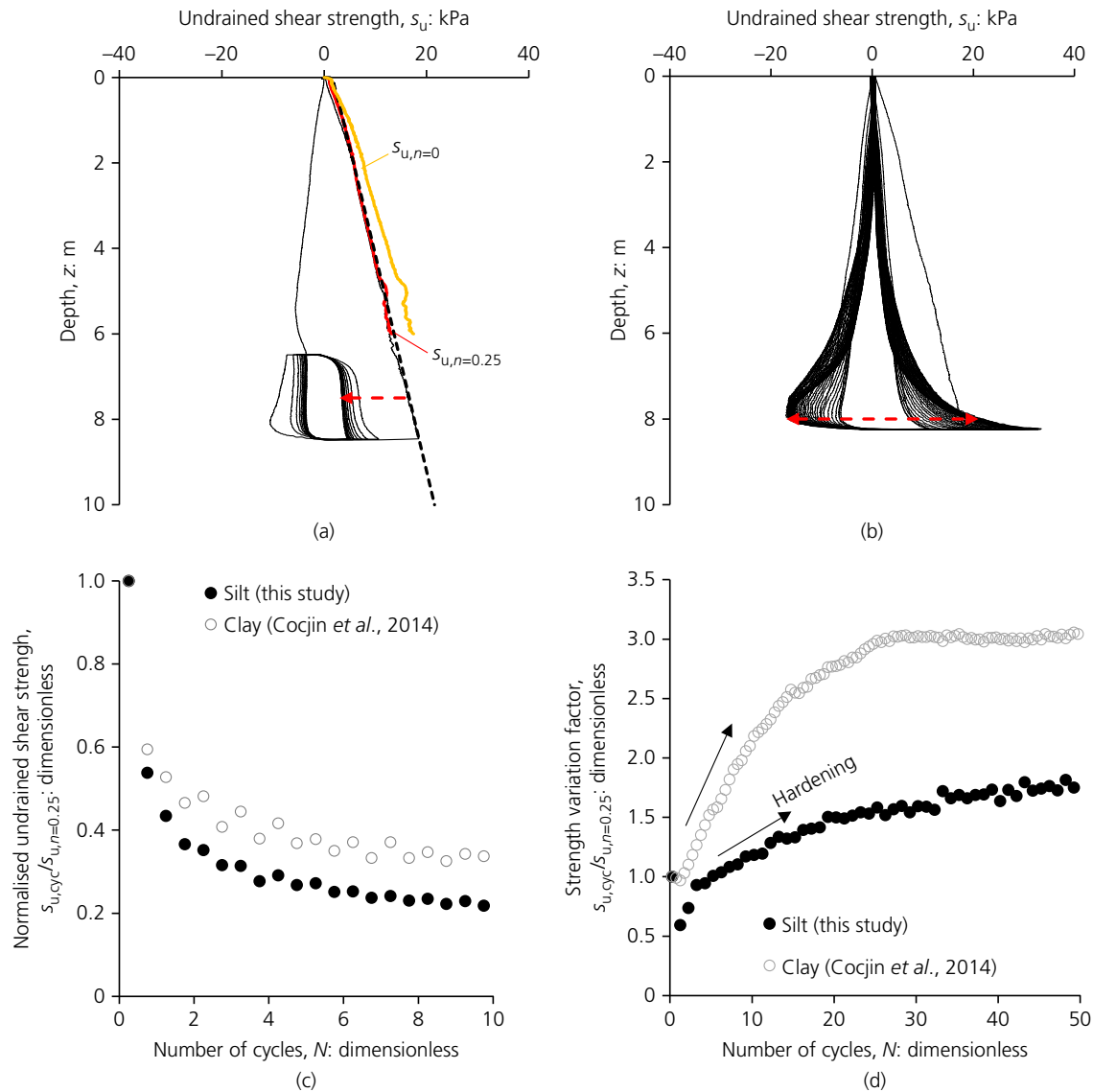


**Figure 6.** Cyclic T-bar penetration tests: (a) strength evolution under continuous cyclic penetration in the calcareous silt; (b) strength evolution of long-running T-bar test in the calcareous silt; (c) strength degradation of the calcareous silt and the kaolin clay; (d) strength enhancement of the calcareous silt and the kaolin clay

corner columns supporting the laser targets fall below the water, but this is considered negligible (comprising only 0.3–0.4% of load change for every 1 mm settlement).

The foundation was first placed at the designated position and carefully touched down in-flight. The vertical operational load ( $V_{op}$ ) was kept constant throughout the test, simulating the weight of the mudmat and the section of the pipe/spool to be supported in the field. Prior to the first slide, the foundation was allowed to consolidate for a period of 4 h (4.5 prototype years), by which time the incremental settlement was

negligible. The mudmat was then slid along the sample surface at a rate of 1 mm/s – sufficiently fast that excess pore pressures were generated – for a distance  $\delta = 0.25L$  to its ‘operational position’ (OP), where it was then left stationary for periods ranging from 780 to 4680 s (0.25–1.5 prototype years) – to simulate different periods of (uninterrupted) operation. The mudmat was then slid back to its (original) ‘shutdown position’ (SD) at the same rate (1 mm/s), to simulate what happens when a subsea system is shut down, leading to cooling and contraction of the attached pipelines. After 8 s of resting (10 prototype days), the foundation was again slid to its



Table 2. Summary of the operative conditions of centrifuge tests on the carbonate silt and the kaolin clay (in prototype)

	Operational load, $V_{op}$ : kN	Initial vertical load mobilisation, $V_{op}/V_{ult0}$ : dimensionless	Pause time at operational position in each cycle, $t_{con}$ : years
S1	200	0.25	0.25
S2	300	0.36	0.25
S3	200	0.25	1.5
S4	200	0.25	1.5 for the 7th, 14th, 28th, ... cycles, 0.25 for the rest
C1	92.5	0.29	0.25
C2	154.5	0.50	0.25
C3	92.5	0.29	1.5

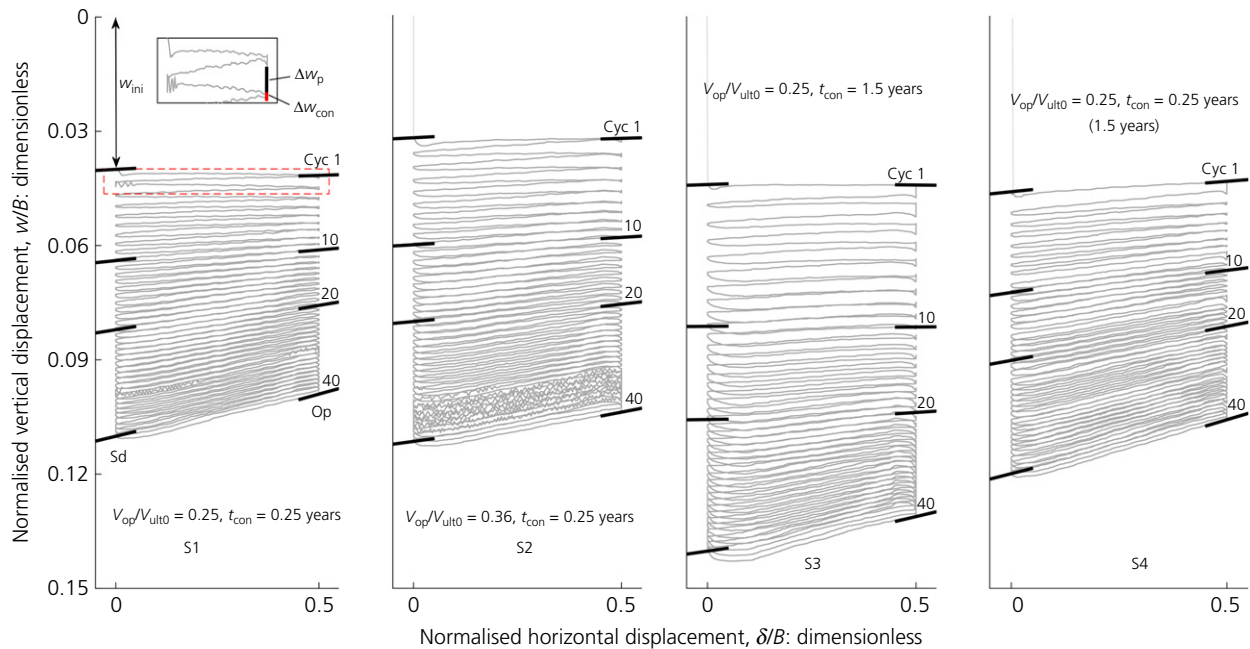


Figure 7. Vertical to horizontal displacement for mobile foundation tests in the calcareous silt: effect of self-weight and consolidation time on vertical settlement

operational position, and the process repeated for 40 cycles, after which a long-term consolidation time of 4.5 h (5 prototype years) was allowed prior to finally lifting of the foundation off the sample surface.

The intervening operational time between the sliding events for all tests in the silt, along with their clay counterparts (C1–C3) from previously performed testing (Cocjin *et al.*, 2014), is summarised in Table 2. The same durations were selected for the silt tests as for the existing clay counterpart tests for comparison purposes.

The operational load and initial vertical load mobilisation ( $V_{op}/V_{ult0}$ , where  $V_{ult0}$  is the initial ultimate bearing capacity) for all seven tests are also given in Table 2, showing tests S1–S3 have a similar vertical load mobilisation as C1–C3. The initial

ultimate bearing capacity  $V_{ult0}$  was estimated based on the intact strength ( $s_{u,n=0}$ ) profile. The surface intercept of the undrained shear strength profile ( $s_{um}$ ) was taken as 1.2 kPa for the calcareous silt, and 0.5 kPa for the kaolin clay. The bearing capacity factor ( $N_c$ ) was calculated using the methodology given by Feng *et al.* (2014), resulting in values of 13.4 and 12.6 for the silt and clay, respectively. The value of  $V_{ult0}$  can be determined as

$$8. \quad V_{ult0} = N_c B L s_{um}$$

Note that the effective vertical load ( $V_{eff}$ ) applied over the base plate of the foundation needs adjusting from the operative vertical load  $V_{op}$ , to account for the fact that the skis increase the footprint area as the foundation settles into the

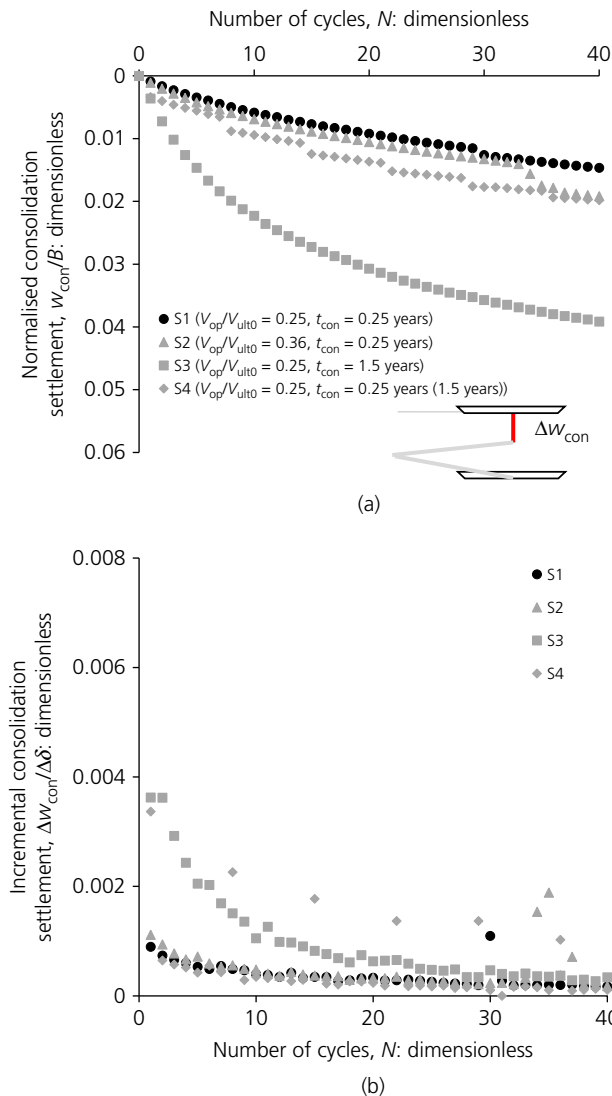


**Figure 8.** Evolution of the normalised consolidation settlement and the incremental consolidation settlement with number of cycles for S1–S4: (a) normalised consolidation settlement; (b) incremental consolidation settlement

soil, as illustrated in Figure 1. In this case,  $V_{eff}$  is estimated as follows:

$$9. \quad V_{eff} = \frac{V_{op}B}{B + 2 \min(h, w) \cot \theta_{mat}}$$

where  $w$  is the settlement of the foundation.

## 6. Model test results and discussion

The results from the tests on silt (S1–S4) are presented in this section, focusing on foundation settlement during periodic

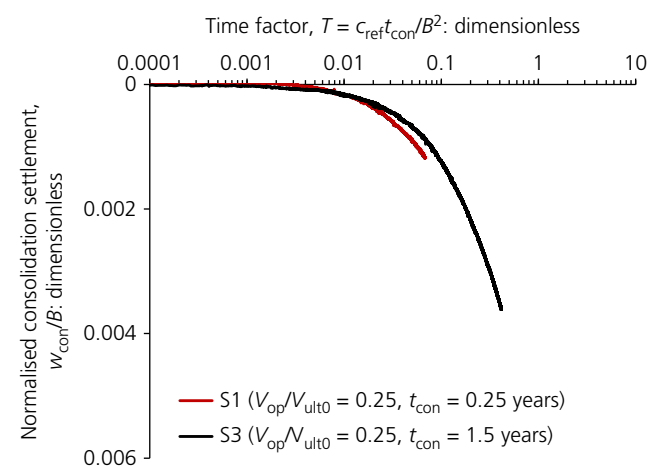


**Figure 9.** Comparison of the consolidation process along with the normalised consolidation time (time factor)  $T = c_{ref} t_{con} / B^2$  in a typical (the first) cycle of tests S1 and S3

sliding and changes in sliding resistance. Where relevant, the results from the calcareous silt tests are compared with the results of tests on kaolin clay presented by Cocjin *et al.* (2014), in order to explore the influence of soil properties on foundation response.

### 6.1 Foundation settlement

The normalised vertical and horizontal displacement observed in tests S1–S4 at specific cycles is shown in Figure 7. The total settlement comprises both the initial settlement (after touch-down) and the sliding-induced settlement.

The initial settlement varied across the tests from  $0.032B$  to  $0.046B$ . It is noted that the test S2, which had the highest load applied to the foundation, recorded the smallest initial settlement – which may reflect a higher OCR at this location, due to its close proximity to the side of the strong box (and hence greater amount of soil removal during scraping due to Coriolis effects).

Sliding-induced settlement develops with the number of applied cycles, and can be attributed to two components: shear settlement ( $w_p$ ) and consolidation settlement ( $w_{con}$ ), as shown in Figure 7. Shear settlement results from combined loading of the foundation at failure (Zhou *et al.*, 2015), while consolidation settlement is induced by the periodic generation and subsequent dissipation of shear-induced excess pore pressure (Cocjin *et al.*, 2017).

The normalised consolidation settlement for tests S1–S4 is plotted against the number of cycles in Figure 8(a). For a given soil type, it is clear that the time period for reconsolidation

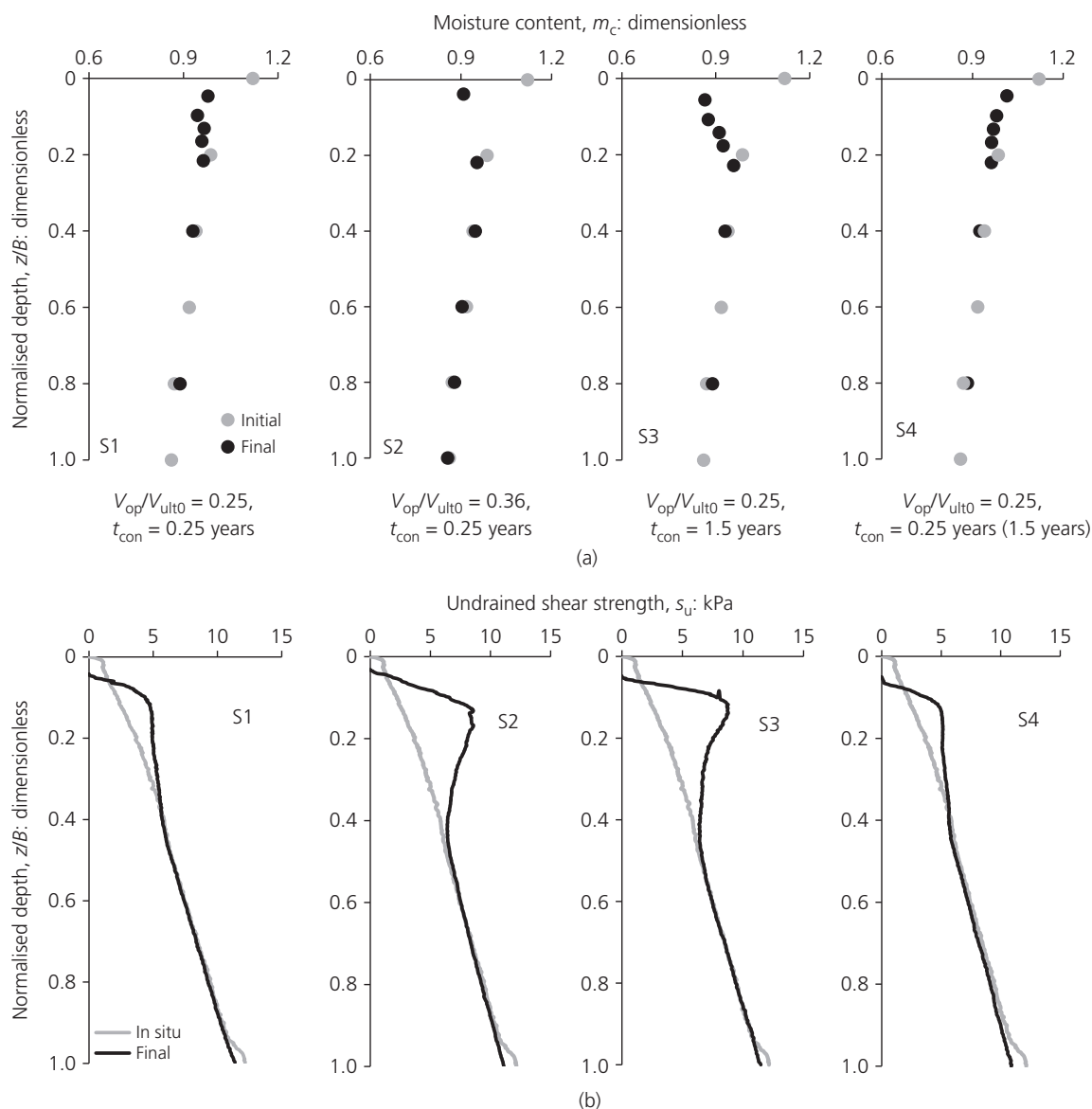


**Figure 10.** Profiles of moisture content and undrained shear strength before and after tests (S1–S4): (a) moisture content; (b) undrained shear strength

and vertical load mobilisation are key influencing factors. The following observations are noted.

- In general, incremental consolidation settlement decreases with cycle number and asymptotes to zero as shown in Figure 8(b), reflecting the fact that the generated excess pore pressure reduces cycle by cycle.
- Test S2 – which was subject to a 44% higher vertical load mobilisation than its counterpart S1 but the same

consolidation time – demonstrated approximately 20% larger accumulated consolidation settlement at the 40th cycle.

- Comparing S1, S3 and S4 – all of which had the same vertical load mobilisation but different intervening reconsolidation times leading to different consolidation settlement. The normalised consolidation settlement of S1 (0.25 years of reconsolidation) and S3 (1.5 years of reconsolidation) observed during a typical cycle (the first cycle) are plotted against normalised consolidation time

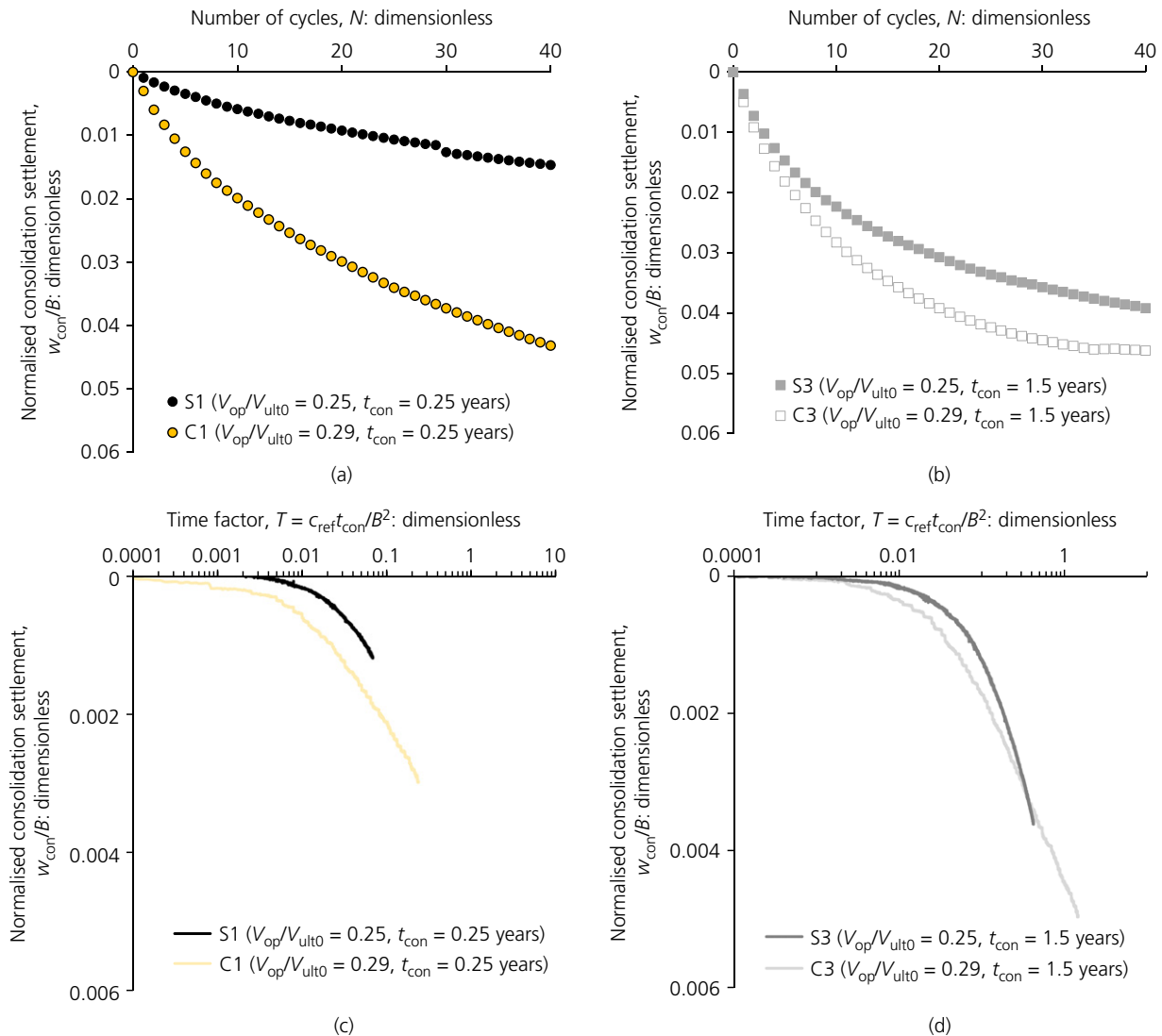


**Figure 11.** Comparison of the whole-life consolidation settlement: (a) S1 against C1, (b) S3 against C3; and corresponding consolidation process along with the normalised consolidation time (time factor)  $T = c_{ref}t_{con}/B^2$  in a typical (the first) cycle: (c) S1 against C1, (d) S3 against C3

(time factor)  $T = c_{ref}t_{con}/B^2$  in Figure 9 to illustrate the reconsolidation process in a single cycle. According to Figure 5(b), approximately 40% consolidation was achieved after 0.25 years, increasing to approximately 90% after 1.5 years.

The consolidation settlement induced by periodic remoulding and reconsolidation is due to the densification of the soil mass at shallow depths as shown in Figure 10(a) in which the moisture content prior to and post model tests (S1–S4) were measured. The densification of the upper soil is also reflected

by the strength variation before and after model tests as shown in Figure 10(b) in which the final strength profile is the average of three T-bar testing locations across each footprint, these being close to the shutdown, mid footprint and operational sides (Figure 2). Longer reconsolidation time and larger vertical load mobilisation are observed to affect the subsoil more dramatically.

Differences between the silt and clay in terms of compressibility (Figure 4) and coefficient of consolidation (Figure 5) lead to different magnitudes of consolidation settlement. The whole-life consolidation settlement of silt cases

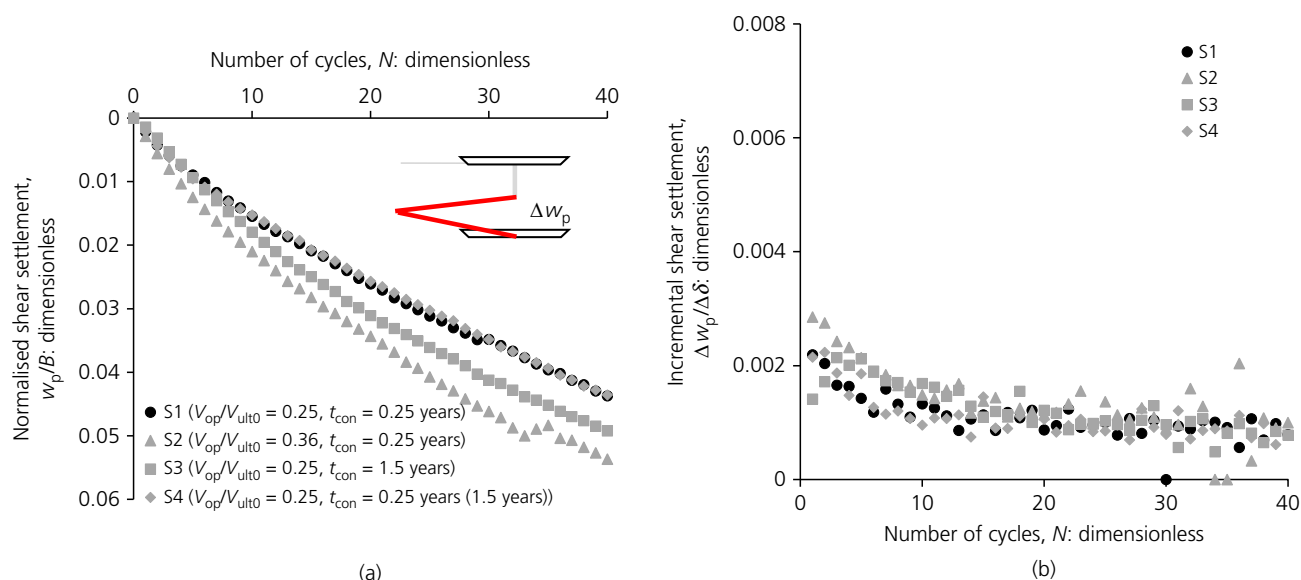


**Figure 12.** Evolution of the normalised shear settlement and incremental shear settlement with number of cycles (S1–S4): (a) normalised shear settlement; (b) incremental shear settlement

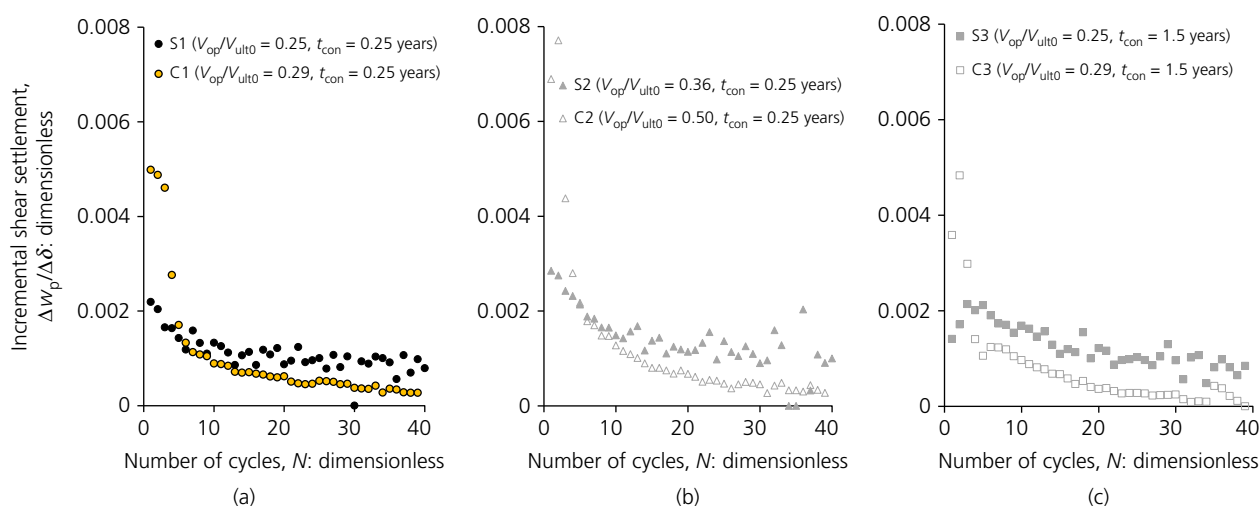


**Figure 13.** Comparison on the evolution of incremental shear settlement in silt and clay: (a) S1 and C1; (b) S2 and C2; (c) S3 and C3

S1 and S3 are compared with their clay counterparts C1 and C3 in Figures 11(a) and 11(b), showing that the silt cases yielded less consolidation settlement than their clay counterparts. Figures 11(c) and 11(d) illustrate that the silt actually experienced a shorter normalised time (i.e. lower degree of consolidation) than the clay in a single reconsolidation period.

Normalised shear settlement for tests in silt S1–S4 is plotted in Figure 12(a) against the number of cycles. Here, it is expected that the vertical load mobilisation has the largest influence and the following is observed.

- In general, the incremental shear settlement, defined as the increment of shear settlement within a sliding cycle

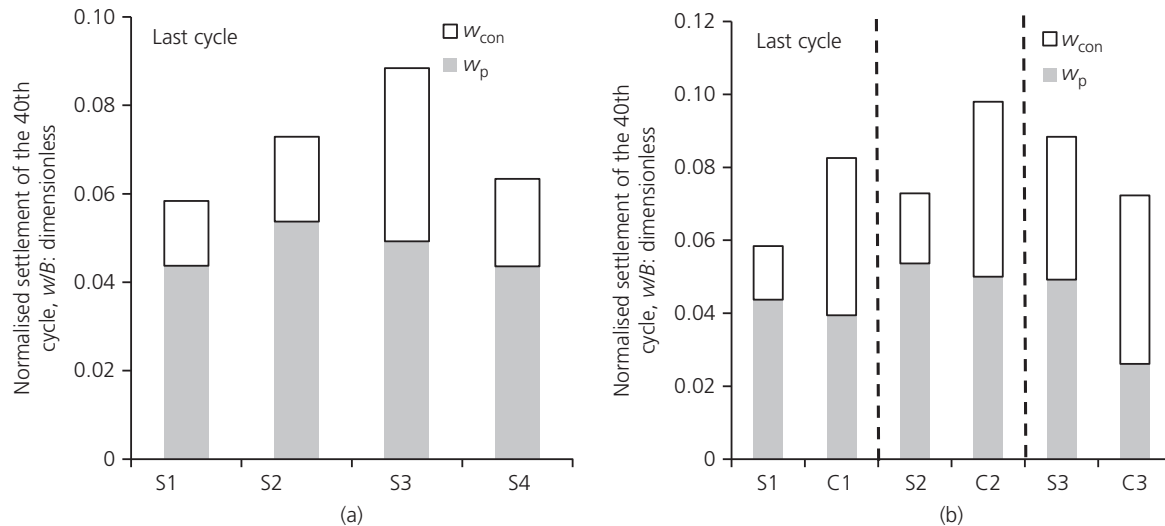


**Figure 14.** Comparison on consolidation and shear settlements at the 40th cycle: (a) for tests in the silt (S1–S4); and (b) comparison of the tests in the silt (S1–S3) and in the clay (C1–C3)

normalised by the sliding distance of a cycle, decreases with cycle number as shown in Figure 12(b). The reduction in incremental shear settlement is related to hardening of the subsoil (Figure 10(b)) and therefore the decrease in the vertical load mobilisation (i.e. reduction in  $V_{op}/V_{ult}$ ) following repeated cycles of remoulding and reconsolidation.

- S2 is 50% heavier than S1, leading to 23% higher shear settlement at the end of the 40th cycle. This trend is consistent with the previous tests in the clay (Cocjin *et al.*, 2014). Under combined loading, larger  $V$  tends to induce failure in deeper subsoil.
- S3, which has a longer reconsolidation time, was expected to yield smaller shear settlement than S1, due to the faster increase in strength in the subsoil (or decrease in  $V_{op}/V_{ult}$ ). However, the opposite result is observed – although the difference appears to be minor, possibly suggesting that other factors (such as strength distribution with depth) are also influencing the induced shear settlement, since the  $H$ – $V$  failure envelope that influences shear settlement development (Deeks *et al.*, 2014; Zhou *et al.*, 2015) is determined by both its size (determined by the magnitude of subsoil being strengthened) and shape (determined by strength distribution).

Figures 13(a)–13(c) show that shear settlement appears to develop differently in the two soil types. Under similar vertical load mobilisation ( $V/V_{ult0}$ ), the shear settlement rate of the silt cases is around half that of their clay counterparts. The shear settlement rate is determined by both the loading state on the  $H$ – $V$  failure envelope ( $V/V_{ult}$ ) and the curvature of the envelope at this loading point, which in turn is controlled by the

strength profile. Therefore, although the silt cases and their clay counterparts have a similar initial loading condition ( $V/V_{ult0}$ ), the curvature of the corresponding envelopes indicates a smaller proportion of vertical to horizontal displacement for the silt due to the higher undrained shear strength ratio. However, the rate of reduction is far slower in the silt than the clay. For example, the initial incremental shear settlement of the silt case S1 is 0.002, dropping by around 50% after 20 cycles. In comparison, the initial incremental shear settlement of its clay counterpart C1 is 0.005 dropping by 90% after 20 cycles (Figure 13(a)). The same trend can be observed in tests C2 and S2 (Figure 13(b)) and C3 and S3 (Figure 13(c)). A slower decrease for S1, S2 and S3 is mainly due to the silt having a lower capacity of strength regain than clay, with reference to Figure 6(d).

Finally, combined shear and consolidation settlement at  $N=40$  is compared for silt tests (S1–S4) in Figure 14(a). It can be seen that longer dissipation periods result in larger consolidation settlement, while the vertical load mobilisation shows the largest influence on shear settlement. Compared to the corresponding tests on clay (as shown in Figure 14(b)), the silt tests generally experience smaller consolidation settlement as a proportion of the total settlement – again reflecting lower compressibility and coefficient of consolidation.

## 6.2 Sliding resistance

Figure 15 shows normalised horizontal resistance against normalised horizontal displacement for tests S1–S4. The following features are observed.

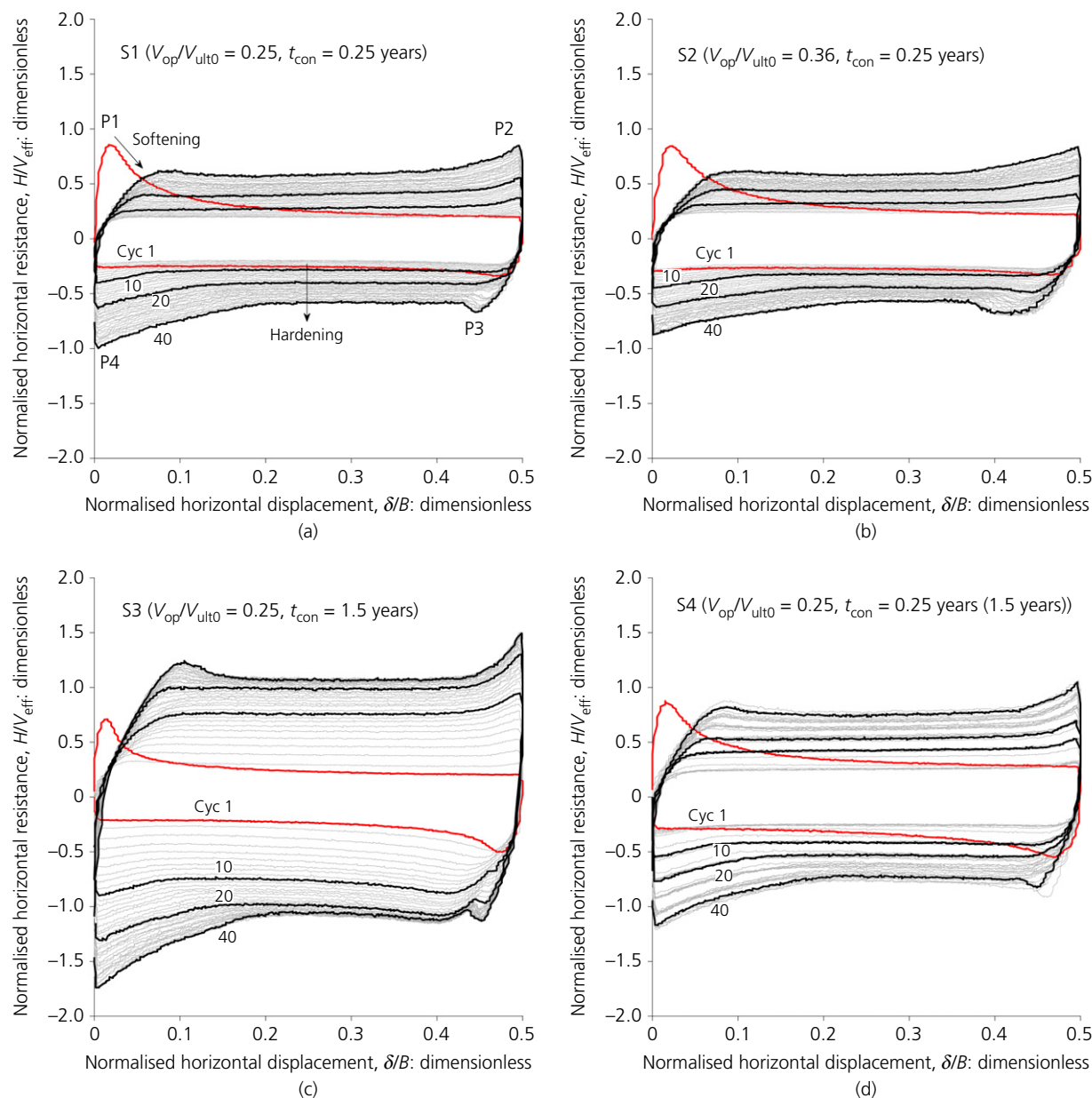


**Figure 15.** Normalised horizontal resistance plotted against normalised horizontal displacement for tests in the silt ((a) S1, (b) S2, (c) S3 and (d) S4): the whole-life resistance evolution of mobile foundation under various reconsolidation times and vertical load mobilisations

- A pronounced peak (P1) is observed on initial sliding, followed by an exponential decay towards a residual sliding resistance – which is seen part way through the slide, prior to engaging soil in the berms at the end of the slide.
- Subsequent peaks (P2 and P4) occur due to the mobilisation of 'dormant' soil berms that accumulate at the extremities of the foundation footprint in response to sliding.
- After being stationary in the operational position, another peak (P3) is observed when the foundation is reversed,

which reflects a combination of an increase in soil strength on the sliding interface and partial mobilisation of the berm as the foundation moves away.

- The residual resistance increases with cycle number, due to an increase in soil strength through periodic monotonic surface shearing and intervening reconsolidation.

The initial peak (P1) is related to the peak undrained shear strength of the soil at the interface, which can be calculated



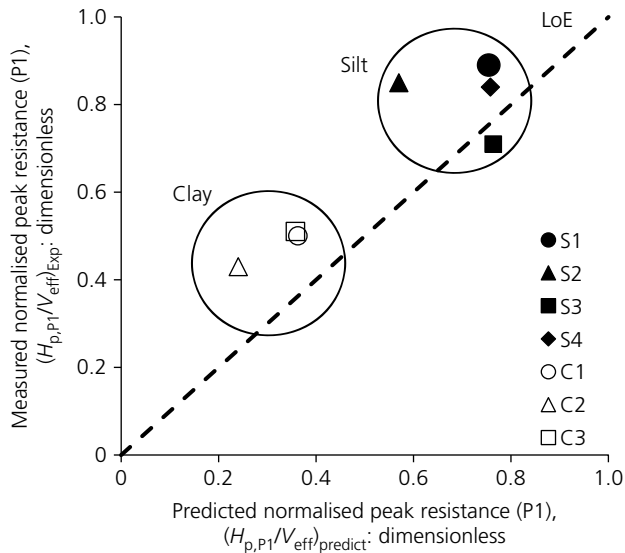


**Figure 16.** Measured normalised initial peak resistance of model tests in the silt (S1–S4) and in the clay (C1–C3) plotted against the calculated values. LoE, line of equivalence

using the undrained strength ratio  $(s_u/\sigma'_v)_{NC,r}$  and Equation 7. The peak horizontal resistance at P1 is then calculated by

$$10. \quad H_{p,P1} = \sigma'_v \left( \frac{s_u}{\sigma'_v} \right)_{NC,r} \text{OCR}^{(\lambda-\kappa)/\lambda} BL$$

The measured normalised peak resistance of P1 for all eight tests is plotted in Figure 16 against the calculated values from Equation 10. In general, Equation 10 provides a good prediction of the initial peak resistances – albeit the predicted values are somewhat lower (12% on average). This slight under prediction could be (partly) attributed to the resistance generated through side shear on the foundation, as well as rate effects (Lehane *et al.*, 2009; Tika *et al.*, 1996) – neither of which have been accounted for. Comparing with the tests on clay, the normalised peak resistance of tests S1–S4 are all higher than those observed in tests C1–C3, reflecting the higher undrained strength ratio of the silt.

The normalised horizontal resistance for the first slide of silt tests is presented in Figure 17(a), and shows that the peak resistance is mobilised within a very short distance and is followed by rapid softening due to soil remoulding. Comparing the typical case S1 with its counterpart C1 in Figure 17(b), it can be observed that longer shearing distance is needed to fully remould the silt than the clay, with  $\delta_{50}$  and  $\delta_{95}$  being 8.8 and 3.4 times that of clay – where  $\delta_{50}$  and  $\delta_{95}$  are the sliding distance to soften the response by 50 and 95%, respectively. Greater sliding distance is required to remould the silt, potentially reflecting difference in soil structure compared with clay.

The increasing residual resistance with cycle number reflects a progressive increase in interface soil strength towards its drained state as shown in Figure 18(a), which is demonstrated through the long-term T-bar testing shown in Figure 6(d). Comparing tests on silt with the longest (S3), intermediate

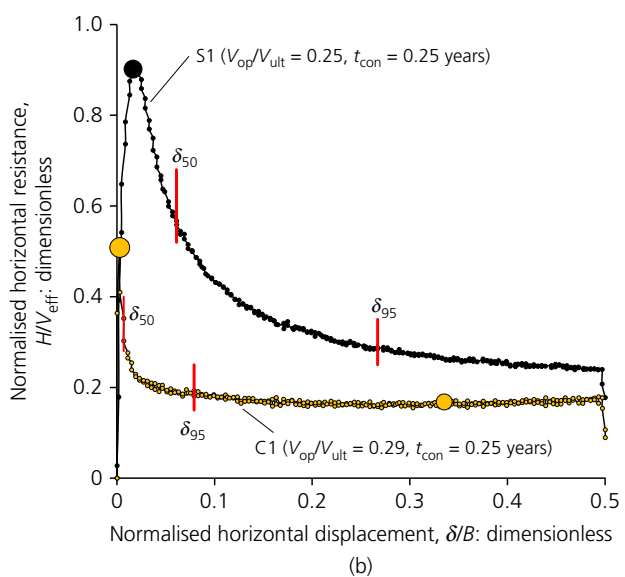
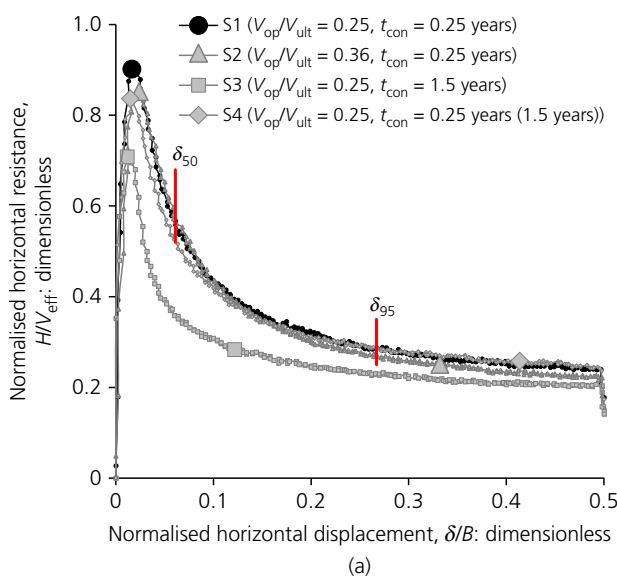


**Figure 17.** Normalised resistance evolution during the first slide: (a) for tests in the silt (S1–S4); and (b) comparison between the typical test in silt (S1) and its clay counterpart (C1)



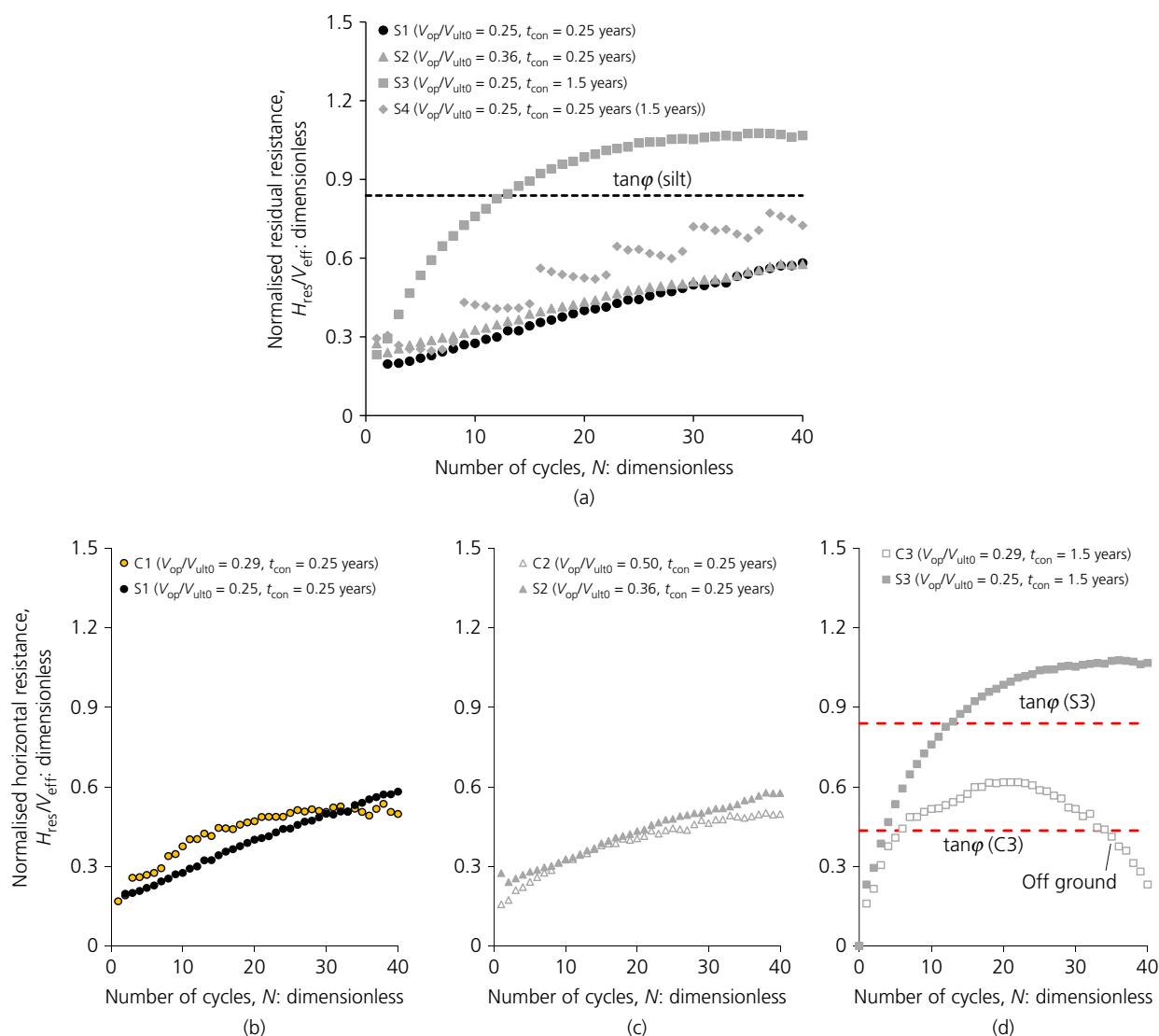


**Figure 18.** Normalised residual resistance evolution with number of sliding cycles: (a) for tests in the silt (S1–S4); comparison between (b) S1 and C1, (c) S2 and C2 and (d) S3 and C3

(S4) and shortest (S1, S2) intervening consolidation time, it can be concluded that the longer the reconsolidation time is, the faster the resistance increases towards the drained state. In contrast, when the intervening consolidation time is the same, tests with different vertical load mobilisation (e.g. S1 and S2) tend to show a comparable response. Soil type also influences strength recovery – comparing tests on the silt (S1–S3) and on the clay (C1–C3) indicates that when the excess pore pressure is allowed to largely dissipate between each cycle, the silt has comparable recovering capacity towards the final drained state (albeit marginally slower) as the clay, as shown in Figure 18(d); while for short-term consolidation cases (S1, C1 or S2, C2) the strength recovery rate of the silt is significantly

slower than that of clay (Figures 18(b) and 18(c)). As seen in the data, after 40 cycles tests C1 and C2 have nearly reached the final (steady) strength, while S1 and S2 have only reached around half of their potential final strength. This shows that the low coefficient of consolidation of the silt controls its recovery rate, which is consistent with the evolution of consolidation settlement as shown in Figure 11.

Comparing tests S3 and C3 in Figure 18(d), it is noted that the maximum normalised residual resistances in both soils exceeds the corresponding drained friction coefficients (written as  $\mu = \tan \phi$ ) calculated from the laboratory testing results shown in Table 1. This is thought to reflect a higher friction angle at

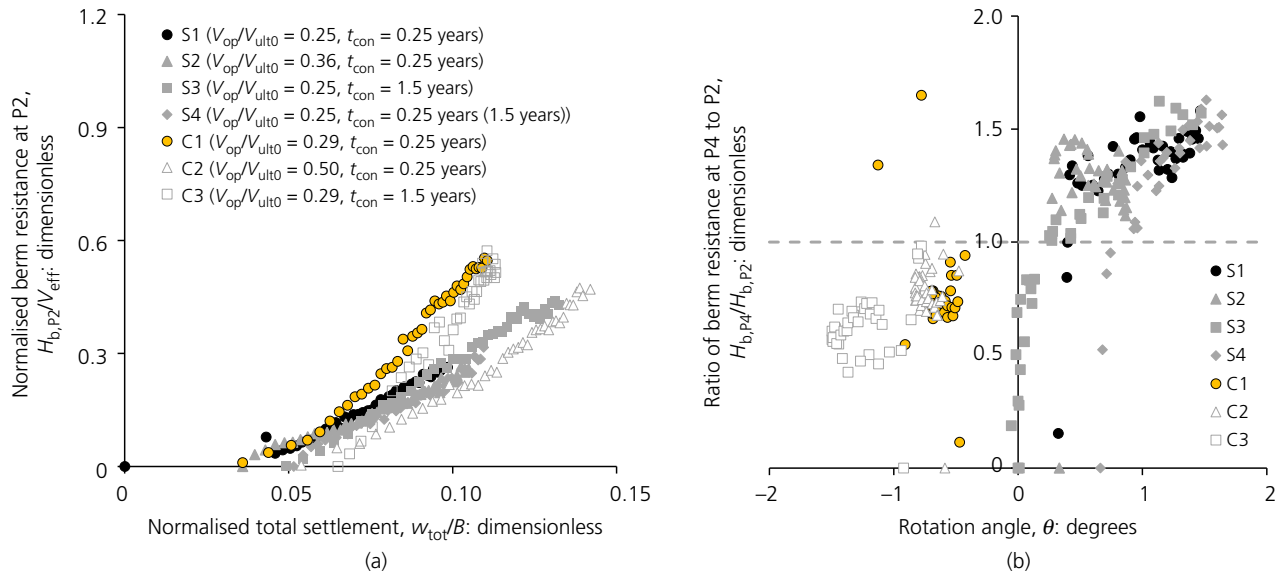


**Figure 19.** Berm resistance evolution for tests in the silt (S1–S4) and in the clay (C1–C3): (a) normalised berm resistance at P2 plotted against normalised settlement; (b) ratio of berm resistances of P4 to P2 plotted against foundation rotation angle

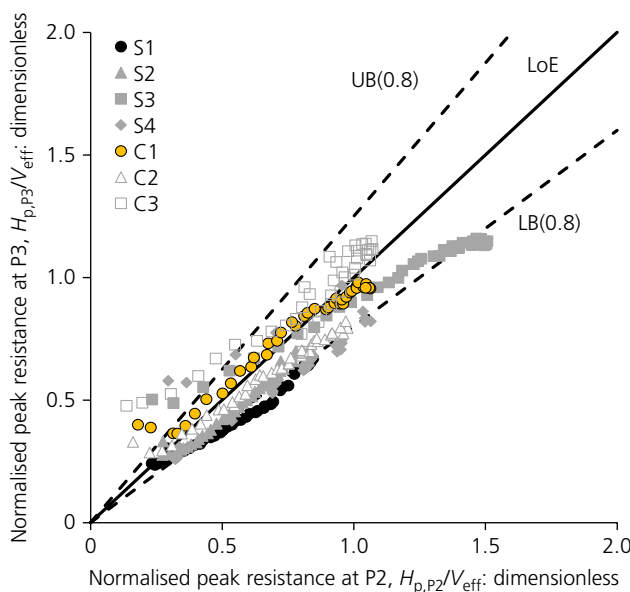


**Figure 20.** Normalised peak resistance at P3 plotted against that of P2 for tests in the silt (S1–S4) and in the clay (C1–C3). UB, upper bound; LB, lower bound

the low applied stress levels, which can be associated with a curved failure envelope. This has been widely observed in various soils (Boukpeti and White, 2017; Maksimovic, 1989; Najjar *et al.*, 2007; Pedersen *et al.*, 2003) – according to the test data for S3 and C3, friction angles of the silt and the clay can

be back-calculated as 47 and 31°, respectively (at operational loads), which are larger than 40 and 23.5° given in Table 1.

Dormant soil berms accumulate due to ploughing of soil in front of the skis, and provide large additional resistance at extremities of the footprint. The normalised resistance at P2 for all seven tests is plotted against normalised total settlement in Figure 19(a), and it appears clear that the berm resistance increases in proportion with the total settlement (and therefore the size of the berms). The size of the soil berms at P2 and P4 also (likely) reflects rotation of the foundation, with the side pitching into the subsoil tending to create a larger berm and greater resistance. The ratio of the maximum berm resistance of P4 to that of P2 is plotted in Figure 19(b) against mudmat rotation angle  $\theta$ , which is defined as positive for the anticlockwise direction.

A final peak (P3) is observed when the mudmat slides from its operational position. The peak resistance at position P3 of all seven tests on both silt and clay is plotted against that observed at position P2 in Figure 20, where it can be seen that the resistances are practically equal (within a margin of error of 20%). While this suggests the P3 peak relates to the remobilisation of the berm for a short distance, before detaching, it is likely that reconsolidation of the soil on the interface (when at the operating position) also contributes to the observed peak.

## 7. Conclusions

Settlement and sliding resistance, which are two critical design aspects of tolerably mobile subsea foundations, have been

explored through centrifuge modelling with an LOC silt and compared with the results on an LOC clay. Settlement, comprising of shear and consolidation components, and sliding resistance, comprising of base and berm resistance, develop during each periodic sliding action and period of intervening consolidation with decreasing rate. The key findings as are follows.

- Shear settlement: the development of shear settlement is influenced by the vertical load mobilisation – dissipation of excess pore pressure due to periodic sliding and reconsolidation events strengthens the subsoil, decreasing the vertical load mobilisation and therefore incremental shear settlement for subsequent cycles. Compared to the clay, tests on the silt experience a slower decrease in incremental shear settlement with cycles of sliding – presumably due to the slower regain of strength.
- Consolidation settlement: the development of consolidation settlement is influenced by both reconsolidation time and vertical load mobilisation. Incremental consolidation settlement decreases with cycle number because the excess pore pressure generated in each cycle reduces as the soil gradually approaches its ultimate drained state. Lower compressibility of the silt at low stress levels and slower dissipation lead to smaller consolidation settlement than corresponding tests in clay.
- Base resistance: the shear stress that provides the base resistance to sliding decreases rapidly from the peak undrained shear strength to a residual strength. The residual strength recovers through periodic reconsolidation, eventually reaching the drained limit that is determined by the friction angle, which tends to be higher than expected, indicating the presence of a curved failure envelope at low stress levels. In general, the strength of the silt increases towards the drained state more slowly than observed in the clay – as the lower consolidation coefficient of silt leads to a reduced degree of consolidation in each operational episode.
- Berm resistance: berms mobilised at the extremities of the sliding footprint lead to local resistance peaks within a single slide. The berm is created by scraping the subsurface soil and is therefore related to the settlement and the rotation of the foundation.

## Acknowledgements

The first author acknowledges his research studentship support from the ARC Industrial Transformation Research Hub for Offshore Floating Facilities and the University of Western Australia. This study was supported by the ARC Industrial Transformation Research Hub for Offshore Floating Facilities, which is funded by the Australia Research Council, Woodside Energy, Shell, Bureau Veritas and Lloyds Register

(grant IH140100012). Phil Watson leads the Shell Chair in Offshore Engineering research team at The University of Western Australia, which is sponsored by Shell Australia. Susan Gourvenec is supported by the Royal Academy of Engineering Chairs in Emerging Technologies Scheme. Xiaowei Feng is supported by the Fundamental Research Funds for the Central Universities (DUT21RC(3)115) and National Natural Science Foundation of China (51890915).

## REFERENCES

- Blanc M, Thorel L, Wallerand R and Stuyts B (2016) Effect of soil profile on the response of a sliding subsea foundation. In *EUROFUGE 2016 3rd European Conference on Physical Modelling in Geotechnics*. Institut Français des Sciences et Technologies des Transports, de l'Aménagement et des Réseaux (IFSTTAR), Nantes, France, pp. 295–300.
- Boukpeti N and White DJ (2017) Interface shear box tests for assessing axial pipe–soil resistance. *Géotechnique* **67**(1): 18–30, <https://doi.org/10.1680/jgeot.15.P112>.
- Bretelle S and Wallerand R (2013) Deep offshore sliding footings – design methodology. In *Proceedings of the 18th International Conference on Soil Mechanics and Geotechnical Engineering*. International Society for Soil Mechanics and Geotechnical Engineering, London, UK, pp. 2331–2334.
- Cathie D, Morgan N and Jaek C (2008) Design of sliding foundations for subsea structures. *Proceedings of the BGA International Conference on Foundations (ICOF2008)*, Dundee, UK, pp. 813–823.
- Chow SH, O'Loughlin CD, Zhou ZF, White DJ and Randolph MF (2019) Penetrometer testing in a calcareous silt to explore changes in soil strength. *Géotechnique* **70**(12): 1160–1173, <https://doi.org/10.1680/jgeot.19.P069>.
- Cocjin MJ (2016) *Whole-life Geotechnical Response of Tolerably mobile Subsea Infrastructure*. Doctoral thesis, The University of Western Australia, Perth, Australia.
- Cocjin MJ, Gourvenec SM, White DJ and Randolph MF (2014) Tolerably mobile subsea foundations – observations of performance. *Géotechnique* **64**(11): 895–909, <https://doi.org/10.1680/geot.14.P.098>.
- Cocjin ML, Gourvenec SM, White DJ and Randolph MF (2017) Theoretical framework for predicting the response of tolerably mobile subsea installations. *Géotechnique* **67**(7): 608–620, <https://doi.org/10.1680/jgeot.16.P137>.
- Corti R, Gourvenec SM, Randolph MF and Diambra A (2017) Application of a memory surface model to predict whole-life settlements of a sliding foundation. *Computers and Geotechnics* **88**: 152–163.
- Deeks AD, Zhou HJ, Krisdani H, Bransby MF and Watson P (2014) Design of direct on-seabed sliding foundations. In *Proceedings of the 33rd International Conference on Ocean, Offshore and Arctic Engineering (OMAE 2014)*. American Society of Mechanical Engineers, New York, NY, USA, paper no. V003T10A024.
- Feng X, Gourvenec S and Randolph MF (2014) Optimal skirt spacing for subsea mudmats under loading in six degrees of freedom. *Applied Ocean Research* **48**: 10–20.
- Gourvenec SM and Feng X (2014) Frontiers in deepwater geotechnics optimizing geotechnical design of subsea foundations. *Australian Geomechanics* **49**(4): 81–99.
- Gourvenec S and Randolph MF (2010) Consolidation beneath Circular Skirted Foundations. *International Journal of Geomechanics* **10**(1): 22–29.

- Lehane BM, O'Loughlin CD, Gaudin C and Randolph MF (2009) Rate effects on penetrometer resistance in kaolin. *Géotechnique* **59**(1): 41–52, <https://doi.org/10.1680/geot.2007.00072>.
- Maksimovic M (1989) Nonlinear failure envelope for soils. *Journal of Geotechnical Engineering* **115**(4): 581–586.
- Nagaraj TS, Pandian NS and Narasimha Raju PSR (1998) Compressibility behaviour of soft cemented soils. *Géotechnique* **48**(2): 281–287, <https://doi.org/10.1680/geot.1998.48.2.281>.
- Najjar SS, Gilbert RB, Liedtke E, McCarron B and Young AG (2007) Residual shear strength for interfaces between pipelines and clays at low effective normal stresses. *Journal of Geotechnical and Geoenvironmental Engineering* **133**(6): 695–706.
- O'Loughlin CD, Cojcin MJ, Gourvenec SM and Stanier SA (2018) A simple approach to multi-degree-of-freedom loading in a geotechnical centrifuge. *Geotechnical Testing Journal* **42**(5): 1150–1168.
- Pedersen RC, Olson RE and Rauch AF (2003) Shear and interface strength of clay at very low effective stress. *Geotechnical Testing Journal* **26**(1): 71–78.
- Randolph MF, Jewell RJ, Stone KJL and Brown TA (1991) Establishing a new centrifuge facility. In *Proceedings of the International Conference on Centrifuge Modelling (Centrifuge 91)*. Balkema, Rotterdam, the Netherlands, pp. 3–9.
- Randolph MF, Gaudin C, Gourvenec SM et al. (2011) Recent advances in offshore geotechnics for deep water oil and gas developments. *Ocean Engineering* **38**(7): 818–834.
- Sahdi F (2013) *The Changing Strength of Clay and Its Application to Offshore Pipeline Design*. Doctoral thesis, The University of Western Australia, Perth, Australia.
- Sahdi F, Gaudin C and White DJ (2014a) Strength properties of ultra-soft kaolin. *Canadian Geotechnical Journal* **51**(4): 420–431.
- Sahdi F, Gaudin C, White DJ and Boylan N (2014b) Interpreting T-bar tests in ultra-soft clay. *International Journal of Physical Modelling in Geotechnics* **14**(1): 13–19, <https://doi.org/10.1680/ijpimg.13.00012>.
- Sahdi F, White DJ and Gaudin C (2016) Experiments using a novel penetrometer to assess changing strength of clay during remolding and reconsolidation. *Journal of Geotechnical and Geoenvironmental Engineering* **143**(4): 06016030, [https://doi.org/10.1061/\(ASCE\)GT.1943-5606.0001637](https://doi.org/10.1061/(ASCE)GT.1943-5606.0001637).
- Stewart DP (1991) A new site investigation tool for the centrifuge. In *Proceedings of the International Conference on Centrifuge Modelling (Centrifuge 91)*. Balkema, Rotterdam, the Netherlands, pp. 531–538.
- Stewart DP (1992) *Lateral Loading of Piled Bridge Abutments due to Embankment Construction*. Doctoral thesis, The University of Western Australia, Perth, Australia.
- Stewart DP and Randolph MF (1994) T-Bar penetration testing in soft clay. *Journal of Geotechnical Engineering* **120**(12): 2230–2235.
- Stuyts B, Wallerand R and Brown N (2015) A framework for the design of sliding mudmat foundations. In *Frontiers in Offshore Geotechnics III* (Meyer V (ed.)). Taylor & Francis Group, London, UK, pp. 807–812.
- Sully JP, Robertson PK, Campanella RG and Woeller DJ (1999) An approach to evaluation of field CPTu dissipation data in overconsolidated fine-grained soils. *Canadian Geotechnical Journal* **36**(2): 369–381.
- Sun L, Lu J, Guo W, Yan S and Jia T (2016) Models to predict compressibility and permeability of reconstituted clays. *Geotechnical Testing Journal* **39**(2): 324–330.
- Teh CI and Houlsby GT (1991) An analytical study of the cone penetration test in clay. *Géotechnique* **41**(1): 17–34, <https://doi.org/10.1680/geot.1991.41.1.17>.
- Tika TE, Vaughan PR and Lemos LJ (1996) Fast shearing of pre-existing shear zones in soil. *Géotechnique* **46**(2): 197–233, <https://doi.org/10.1680/geot.1996.46.2.197>.
- Wallerand R, Stuyts B, Blanc M, Thorel L and Brown N (2015) A design framework for sliding foundations: centrifuge testing and numerical modelling. *Offshore Technology Conference, Houston, TX, USA*, paper no. OTC-25978-MS.
- White DJ, Gaudin C, Boylan N and Zhou H (2010) Interpretation of T-bar penetrometer tests at shallow embedment and in very soft soils. *Canadian Geotechnical Journal* **47**(2): 218–229.
- Wroth CP (1984) Interpretation of in situ soil tests. *Géotechnique* **34**(4): 449–489, <https://doi.org/10.1680/geot.1984.34.4.449>.
- Zhou H and Randolph MF (2009a) Numerical investigations into cycling of full-flow penetrometers in soft clay. *Géotechnique* **59**(10): 801–812, <https://doi.org/10.1680/geot.7.00200>.
- Zhou H and Randolph MF (2009b) Resistance of full-flow penetrometers in rate-dependent and strain-softening clay. *Géotechnique* **59**(2): 79–86, <https://doi.org/10.1680/geot.2007.00164>.
- Zhou H, Krisdani H, Maujean R and Deeks AD (2015) System integration of direct on-seabed sliding foundations. In *Frontiers in Offshore Geotechnics III* (Meyer V (ed.)). Taylor & Francis Group, London, UK, pp. 825–830.
- Zhou Z, O'Loughlin CD and White DJ (2019) An effective stress analysis for predicting the evolution of SCR-seabed stiffness accounting for consolidation. *Géotechnique* **70**(5): 448–467, <https://doi.org/10.1680/jgeot.18.P313>.
- Zhou Z, O'Loughlin CD, White DJ and Stanier SA (2020a) Improvements in plate anchor capacity due to cyclic and maintained loads combined with consolidation. *Géotechnique* **70**(8): 732–749, <https://doi.org/10.1680/jgeot.19.T1.028>.
- Zhou Z, White DJ and O'Loughlin CD (2020b) The changing strength of calcareous silt: parallel penetrometer and foundation tests with cyclic loading and reconsolidation periods. *Canadian Geotechnical Journal* **57**(11): 1664–1683.

## How can you contribute?

To discuss this paper, please email up to 500 words to the editor at [support@emerald.com](mailto:support@emerald.com). Your contribution will be forwarded to the author(s) for a reply and, if considered appropriate by the editorial board, it will be published as discussion in a future issue of the journal.

*International Journal of Physical Modelling in Geotechnics* relies entirely on contributions from the civil engineering profession (and allied disciplines). Information about how to submit your paper online is available at [www.icevirtuallibrary.com/page/authors](http://www.icevirtuallibrary.com/page/authors), where you will also find detailed author guidelines.